Conformal Parallel Plate Waveguide Polarizer Integrated in a Geodesic Lens Antenna

Freysteinn V. Vidarsson, *Graduate Student Member, IEEE*, Oskar Zetterstrom, *Graduate Student Member, IEEE*, Astrid Algaba-Brazález, Nelson J. G. Fonseca, *Senior Member, IEEE*, Martin Johansson, *Senior Member, IEEE*, Lars Manholm, and Oscar Quevedo-Teruel, *Senior Member, IEEE*

***Abstract*— Here, we propose a low-profile polarizing technique integrated in a parallel plate waveguide (PPW) configuration, compatible with fully metallic geodesic lens antennas. The geodesic shape of the antenna is chosen to resemble the operation of a Luneburg lens. The lens is fed with 11 waveguide ports with 10° separation producing 11 switchable beams in an angular range of ±50°. Two metallic polarizing screens are loaded into the aperture of the antenna to rotate the electric field from a vertical linear polarization, which is the polarization of the transverse electromagnetic (TEM) mode supported in the lens, to a +45° linear polarization. Since the polarizing unit cells are integrated into the aperture of the antenna, the final design is compact. In addition, the size of the polarizing unit cells is about 0.55λ at the central frequency of operation making the antenna suitable to produce an array formed of stacked lenses. A prototype of the antenna in the K_a-band was manufactured and tested, verifying the performance obtained in simulations.**

***Index Terms*— Beam scanning, fully metallic, geodesic lens, Luneburg lens antenna, polarization transformation.**

I. Introduction

THE demands for high data rates, capacity, and low latency in future generations of mobile networks (5G and 6G) can be fulfilled by moving toward higher operating frequencies [1], more specifically within the millimeter-wave range and sub-THz bands [2], [3], [4]. However, using higher frequencies, both path loss and material losses increase creating a need for high-gain and efficient antennas [5], [6]. Consequently, beam switching is an essential feature to achieve acceptable angular coverage [7]. Antenna arrays are one popular option when highly directive beams are needed in a wide angular range. The beam steering in arrays can be achieved electronically, mechanically [8], or as a combination of the two [9]. However, at high frequencies, the required feeding network for electronically scanned arrays becomes complex and lossy [10]. Losses in the feeding network can be avoided by having a fully mechanically scanned array; this, however, results in a slower scanning speed and a bulky design [8].

Lens antennas have received attention due to their wideband behavior and their ability to produce high-gain switchable beams over a wide angular range without requiring a complex feeding network [11]. Lens antennas were broadly studied in the 1940s–1960s [12], [13] but deemed unpractical at low frequencies due to their large size and high manufacturing cost. Nevertheless, when the frequency increases, the physical size of the lenses is reasonably small while being large in terms of wavelength meaning they can provide high-gain beams [14]. The Luneburg lens [15] is an interesting case for antenna designs since it can be used to produce multiple beams in a large angular range and a wide frequency bandwidth. The planar version of the Luneburg lens is a compact device with a wide scanning range in one plane [16]. The required graded refractive index of the Luneburg lens can be achieved using dielectrics [17], metasurfaces [18], [19], [20], [21] or geodesic surfaces [22], [23], [24], [25], [26].

Geodesic surfaces can mimic the refractive index of rotational symmetric lenses using a profiled surface [22], [27], [28]. By making use of the direction orthogonal to the beamforming plane, a parallel plate region can be deformed into a geodesic surface [29]. The resulting surface is a device that can be easily manufactured and eliminates the need for inhomogeneous materials to achieve the required refractive index of the lens. However, this is done at a cost of an increased height of the lens, hence sacrificing compactness. Solutions to this problem have been addressed in [23], [24], and [30].

Investigating ways to implement dual-polarized lens antennas is of special interest for both the satellite and terrestrial communication systems, where it is needed to transmit or receive dual-polarized signals to or from the antennas [31], [32]. Polarization manipulation is indeed a challenge in fully metallic parallel plate waveguide (PPW) beamformers due to the supported fundamental modes. This is less challenging in 3-D lenses since the polarization can be readily implemented in the feed or before the lens [33], [34]. The typical solution in PPW beamformers is to have an array of polarizing unit cells at some distance away from the beamformer. One such designs is proposed in [35] where the polarizer array transformed the linear polarization of the PPW beamformer to circular

Manuscript received 23 June 2021; revised 30 June 2022; accepted 20 July 2022. Date of publication 4 October 2022; date of current version 17 November 2022. This work was supported by the Strategic Innovation Program Smarter Electronics System—a joint venture of Vinnova, Formas and the Swedish Energy Agency, under Project High-Int 2019-02103. *(Corresponding author: Freysteinn V. Vidarsson.)*

Freysteinn V. Vidarsson, Oskar Zetterstrom, and Oscar Quevedo-Teruel are with the Division of Electromagnetic Engineering, KTH Royal Institute of Technology, 114 28 Stockholm, Sweden (e-mail: fvvi@kth.se).

Astrid Algaba-Brazález, Martin Johansson, and Lars Manholm are with Ericsson Research, Ericsson AB, 417 56 Gothenburg, Sweden.

Nelson J. G. Fonseca is with the Antenna and Sub-Millimetre Waves Section, European Space Agency, 2200 AG Noordwijk, The Netherlands.

Color versions of one or more figures in this article are available at https://doi.org/10.1109/TAP.2022.3209266.

Digital Object Identifier 10.1109/TAP.2022.3209266

polarization. In addition, the polarizer array acted as a reflector which could be mechanically steered. However, for some antenna applications it is not suitable to use big reflectors for polarization transformation, and hence compact solutions are needed [36].

Using septum polarizers integrated within a square waveguide is one method to achieve circular polarization for a PPW beamformer in a compact way [37]. In septum polarizers, a square waveguide is fed by two rectangular waveguides, each of which supports one propagating mode. The square waveguide, on the other hand, supports two orthogonal propagating modes. The polarization of the incident signal is converted by adjusting the phase between these two orthogonal propagating modes. In [38], septum polarizers integrated within a square waveguide were used to generate circular polarization in a PPW multiple beam quasi-optical beamformer operating in K_a-band. This was done by discretizing the aperture of the beamformer which results in a reduced scanning range. In [39], a modification of the standard septum is used where the vertical walls added to create square waveguides are removed, and the stepped septum is replaced with a saw-like design based on periodic teeth. This results in a continuous aperture avoiding the problem of the limited scanning range in [38]. However, this concept comes at a cost of limited bandwidth because the TEM mode is maintained in the teeth area, while the orthogonal mode is a TE mode. The two modes have very different propagation characteristics, meaning the required phase shift between both the modes will only be obtained at the design central frequency.

In this article, we propose a low-profile solution to obtain a linear-to-linear polarization transformation in a fully metallic geodesic Luneburg lens operating at the K_a-band. The concept is based on a PPW polarizer with wideband matching to free space and polarization conversion. The implementation of the presented solution relies on thin polarizing sheets that may be bent to adapt to the curvature of the aperture (e.g., combination with a Luneburg or geodesic lens), hence supporting wide scanning. The polarizing screen provides linear polarization rotation ($\pm 45°$) to enable polarization diversity from a stack of PPW beamformers. Even though this concept is being demonstrated using a geodesic Luneburg lens, this method can be applied to any kind of PPW beamformer such as a shaped parallel plate delay lens [40] or a pillbox antenna [11], [41].

This article is organized as follows. In Section II, the geodesic surface of the lens antenna is introduced, and a flare and feeding design are presented. This section also reports the simulation results of the whole lens antenna. Section III is dedicated to the polarizing unit cell design and a discussion on how to integrate the polarizer together with the antenna. Section IV includes the experimental results of the integrated antenna, and finally, the main conclusions are drawn in Section V.

II. Water Drop Lens Antenna Design

A. Geodesic Lens Design

The Luneburg lens is a rotationally symmetric graded index lens [15]. The refractive index of the lens varies from $(2)^{1/2}$ in the center to 1 at the border of the lens. When the Luneburg lens is excited with a cylindrical source on its boundary, it produces a wave with a planar phase front in the diametrically opposite direction of the lens. Due to the rotational symmetry, when this lens is integrated in an antenna, the scan losses are low and scanning is readily achieved by feeding the lens at different locations along its boundary, eliminating the need for a complex feeding network.

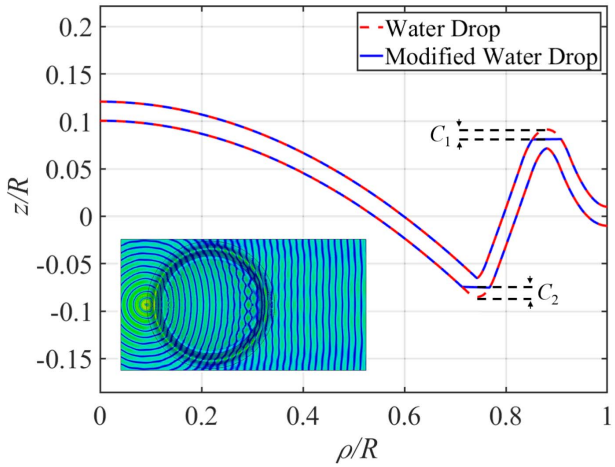

Fig. 1. Surface profile of the water drop lens. Red dashed lines show the normalized profile of the water drop lens, and the blue solid line shows the modified water drop profile which is used in this work.

In [29], a surface equivalence of the Luneburg lens is proposed and implemented with a PPW which is deformed to mimic the gradient refractive index of the Luneburg lens. The resulting PPW lens is referred to as a geodesic Luneburg lens. The main advantage of the geodesic lens is that it can be realized using a homogeneous material, such as vacuum or air.

One disadvantage of the geodesic lens is the required height of the equivalent surface which is a third of its diameter. This issue is addressed in [30] where it was proposed to fold the geodesic surface to achieve a more compact device while preserving the optical characteristics of the lens. Such structure was not studied again in the literature until the recent implementation presented in [23], where a height reduction of 2.5 from the conventional geodesic Luneburg lens is reported.

In [24], a rigorous design procedure for implementing a compact geodesic lens is described. The resulting lens is referred to as a water drop lens. We have followed such a design procedure in the current investigation. The shape of the designed water drop lens used in this work is shown in Fig. 1. The dashed red lines show the surface profile of the water drop lens. The distance between parallel plates is 2 mm, which is about 0.2λ at the central frequency. This distance was chosen so only the TEM mode can propagate within the frequency range of interest. In Fig. 1, the solid blue lines show modifications applied to the initial profile, in terms of cuts, to improve the matching at the folding points. These cuts are $C_1 = 0.5$ mm and $C_2 = 0.35$ mm. Since they are small, the beamforming capability of the lens is not affected. This lens is designed to operate from 25 to 31 GHz. The diameter of the lens is chosen as 107 mm, which is approximately 10λ at the center frequency. The inset of Fig. 1 shows how the lens

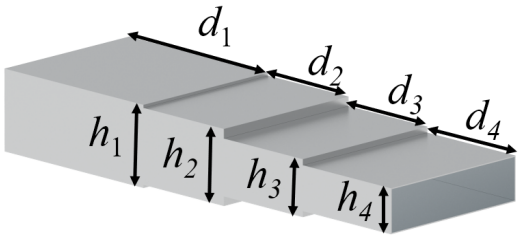

Fig. 2. Stepped waveguide for the transition from WR28 to the PPW lens.

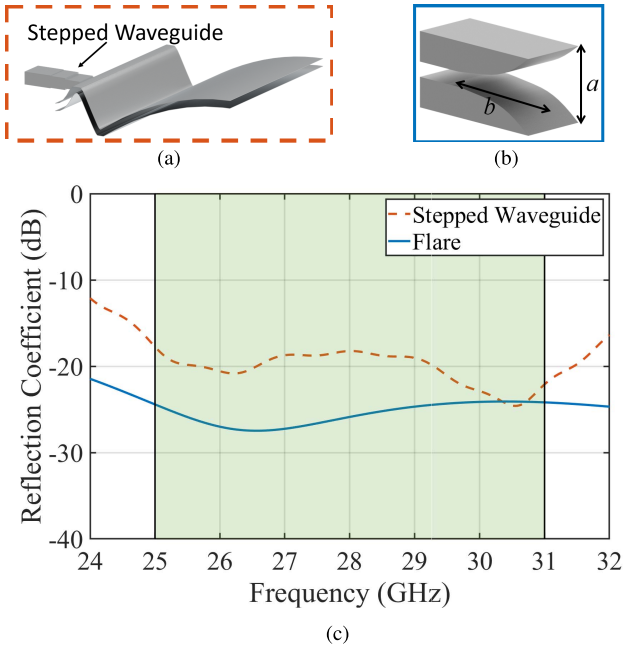

Fig. 3. Flare and feeding design. (a) Simulation model of the stepped waveguide, including the initial part of the lens's profile. Dimensions for the stepped waveguide are $d_1 = 10$ mm, $d_2 = 4.6$ mm, $d_3 = 11.2$ mm, $h_1 = 3.56$ mm, $h_2 = 3.3$ mm, $h_3 = 2.5$ mm, and $h_4 = 2$ mm. (b) Flare design with exponential tapering. Dimensions of the flare are $a = 10$ mm and $b = 14.5$ mm. (c) Reflection coefficients of the designed feeding and flare.

transforms a cylindrical wave excited at its border to a planar wavefront in the opposite direction.

B. Flare and Feeding Design

To feed the water drop lens, we use a standard WR28 waveguide. Since the distance between parallel plates in the water drop lens does not match the height of a WR28, a stepped waveguide transition is needed, as illustrated in Fig. 2. To reduce the computational time of the simulations, only a portion of the lens is included in the optimization of the stepped waveguide, as shown in Fig. 3(a).

On the other side of the lens, a flare design is required to allow efficient radiation to free space. The flare has an exponential tapering from the height of the parallel plate of the lens, 2 mm, to a final aperture height of 10 mm which is approximately one wavelength at the central frequency. The reflection coefficients for the designed feeding and flare are depicted in Fig. 3(c). The flare has a reflection coefficient below -20 dB in the frequency band of interest, and the feeding reflection coefficient is below -18 dB.

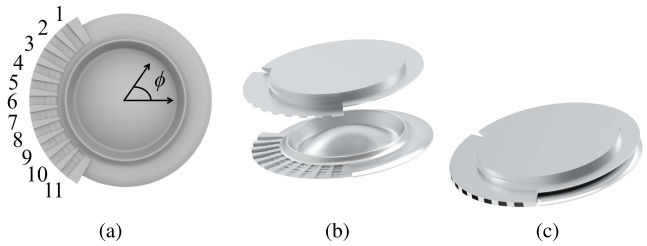

Fig. 4. Designed water drop lens antenna. (a) Top view of the bottom plate showing the 11 waveguide feeds. (b) Exploded view of the top and bottom plates of the antenna. (c) Assembled top and bottom plates of the antenna.

C. Water Drop Lens Antenna

Fig. 4(a) shows a top view of the bottom plate of the lens antenna integrated with the feeding and flare described in Section II-B. Eleven waveguide feeds are placed with 10° spacing allowing for a scanning range of ±50°. The flare covers all the radiating aperture up to the walls of ports 1 and 11. Fig. 4(a) and (c) shows how the two beamforming plates, when combined, form the geodesic lens.

The simulated results for some selected ports with the *time-domain solver* of *CST Microwave Studio* are represented in Fig. 5. The S-parameters are shown in Fig. 5(a), demonstrating that all the reflection coefficients are below -16 dB and port-to-port coupling is below -19 dB in the frequency band of interest. The simulated 2-D radiation patterns for ports 1, 6, and 11 at 25, 28, and 31 GHz, respectively, are shown in Fig. 5(b). The antenna produces directive beams, and the performance is stable over the scanning range and the frequency band. The sidelobe levels are as low as -20 dB at the highest frequency, 31 GHz, and never higher than -14 dB at the lowest frequency, 25 GHz. Fig. 5(c) shows the maximum directivity of all 11 feeding ports at 25, 28, and 31 GHz. A low directivity variation is observed between pointing directions with a maximum of 0.2 dB.

III. Parallel Plate Integrated Polarizer

A. Polarization Diversity in PPW Beamformers

Polarization transformation in fully metallic PPW beamformers introduces challenges, mainly due to the fundamental modes supported in such devices. The height of the PPW used to form the required geodesic surface must be chosen so that only the TEM mode is allowed. Introducing the second mode, the TE_{01} mode, would not result in the desired performance of the lens due to the dispersive relationship between the two modes. This means that any polarization transformation must be done after the beamforming stage of the antenna. Techniques to achieve dual-polarized PPW antennas are of special interest for both the satellite and terrestrial communication systems as polarization diversity doubles the link capacity for a given frequency bandwidth allocation. Here, we want to investigate a way to transform the nominal vertical polarization of the TEM mode supported in the geodesic Luneburg lens to a +45° linear polarization, so polarization diversity may be achieved stacking two lenses with polarization transformation of +45° and −45°.

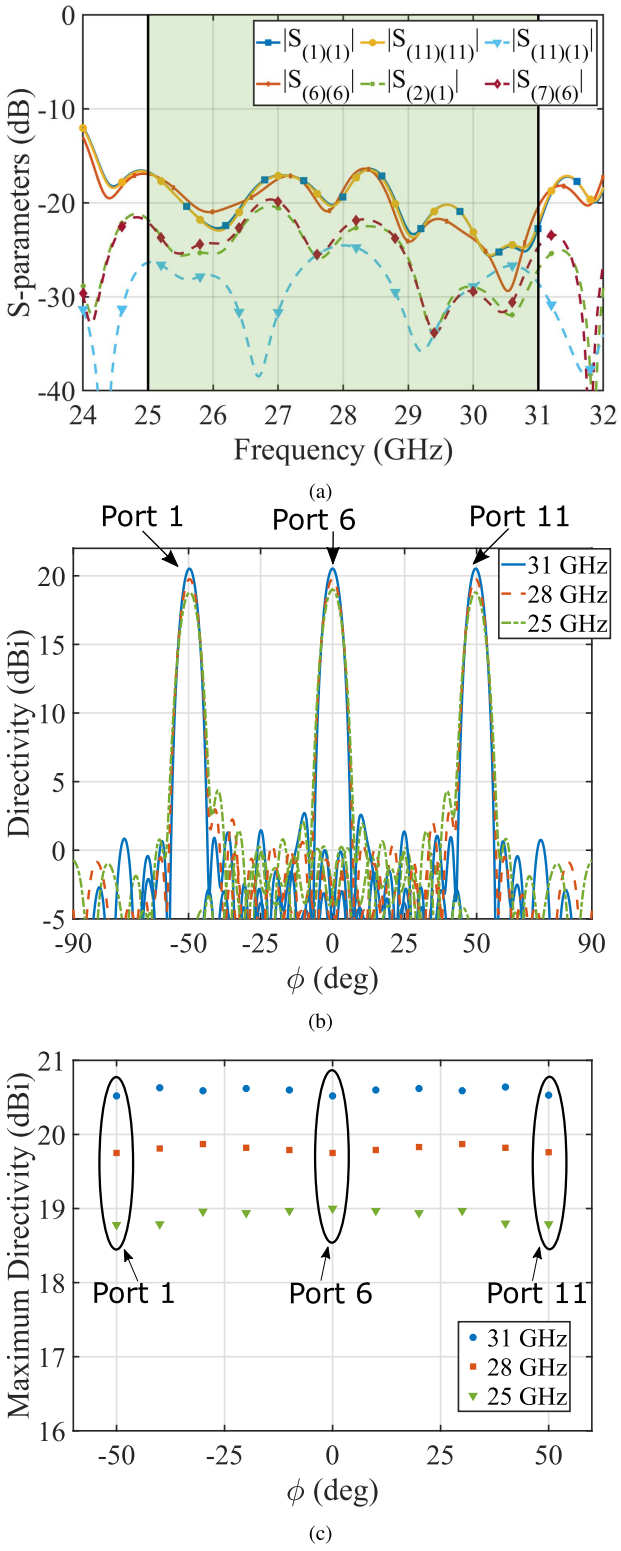

Fig. 5. Simulation results for the conventional water drop lens. (a) Selected S-parameters. (b) Radiation pattern for ports 1, 6, and 11 at 25, 28, and 31 GHz. (c) Maximum directivity of all the ports at 25, 28, and 31 GHz.

In this article, we propose a compact polarizer that does not limit the bandwidth or the beam scanning capabilities of the antenna.

B. Complementary Split-Ring Resonators

In [42], it is shown that twist-symmetric complementary split-ring resonators (CSRRs), perforated from a sheet of aluminum, can be used to construct a flat fully metallic lens. This type of perforated sheets with CSRRs can also be used to generate polarization transformation with a wideband performance as demonstrated in [43]. In the aforementioned studies, the CSRRs were used in a 2-D array configuration. In this work, we load the CSRRs in a PPW with a 1-D design for polarization transformation in a geodesic Luneburg lens.

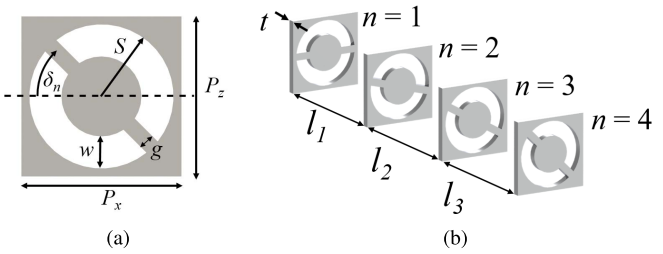

Fig. 6. CSRR. (a) Front view of one unit cell when the center bar has been rotated by an angle δ_n. (b) CSRR in a layered configuration.

The CSRR unit cell is shown in Fig. 6(a). The unit cell is characterized with a rectangular section with dimensions P_z and P_x, a center bar of width g, and a slot of width w made by two concentric circles with radii S and S–w. The center bar is rotated by an angle δ_n, so the electric field traveling through the CSRR rotates as well. This rotation of the electric field is smoothly achieved in steps as illustrated in Fig. 6(b), where the center bar of every consequent unit cell is rotated by an incremental value. This polarization conversion in steps improves the matching between screens when rotating the center bar. This means that the fewer the screens, the larger the reflections. A study to determine the minimum required number of polarizing screens to achieve a good matching to free space must be carried out.

C. Design Procedure for the Polarizer

In [42] and [43], the CSRRs were studied at a unit cell level, as commonly done when designing a 2-D transmit array. That design environment does not fit the purpose of this work since the polarizer will not be used in a planar configuration but rather in a PPW environment. The CSRRs will be repeated in the x-direction but there is only one CSRR unit cell in the z-direction. To mimic this environment, the polarizer is analyzed directly in its PPW environment as shown in Fig. 7, where a PPW is loaded with $n = 4$ polarizer screens. For each screen, the unit cell is repeated 16 times in the x-direction. In this way, when the PPW is excited at the waveguide port with a TE_{10} mode, the excited wave will behave like a quasi-TEM wave. Furthermore, with 16 unit cells, the width of this simulation model is roughly the same as the lens diameter. The PPW height is tapered from the height of the PPW of the lens to the height of the CSRR unit cells. As can be seen in the cross-sectional view of the loaded PPW in Fig. 7(b), the polarizer screens are placed in grooves for assembly purposes.

Two, three, and four polarizer screens are considered for the study, as shown in Fig. 8(a). In all the cases, the outer radius and the slot width are kept constant as $S = 2.65$ mm and $w = 1$ mm, respectively. The lateral dimensions are $P_x = P_z = 5.7$ mm, roughly 0.55λ at the central frequency. These lateral dimensions were chosen to be small enough so the final design is suitable for a vertical stacked antenna array. It must

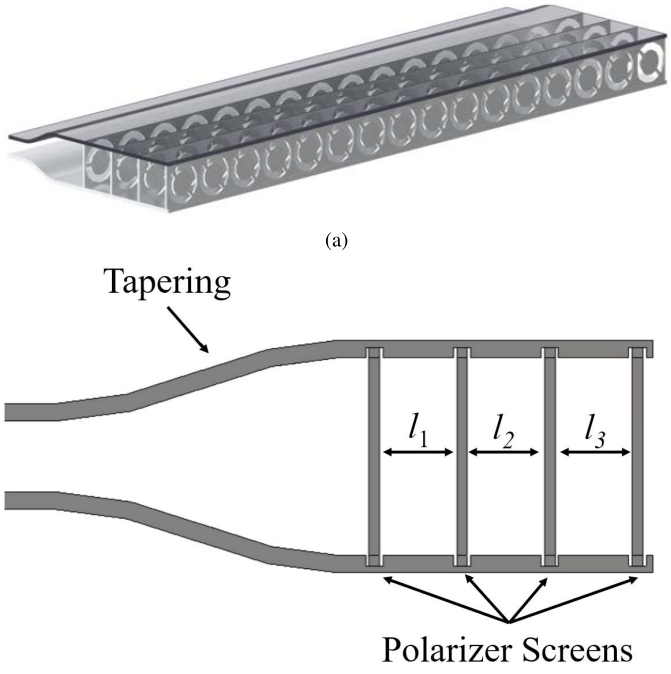

Fig. 7. PPW loaded with CSRRs. (a) PPW with tapering from the height of the lens to the height of the CSRRs. (b) Cross-sectional view of the loaded PPW showing the placement grooves that will be milled into the flare of the antenna to hold the screens with CSRRs.

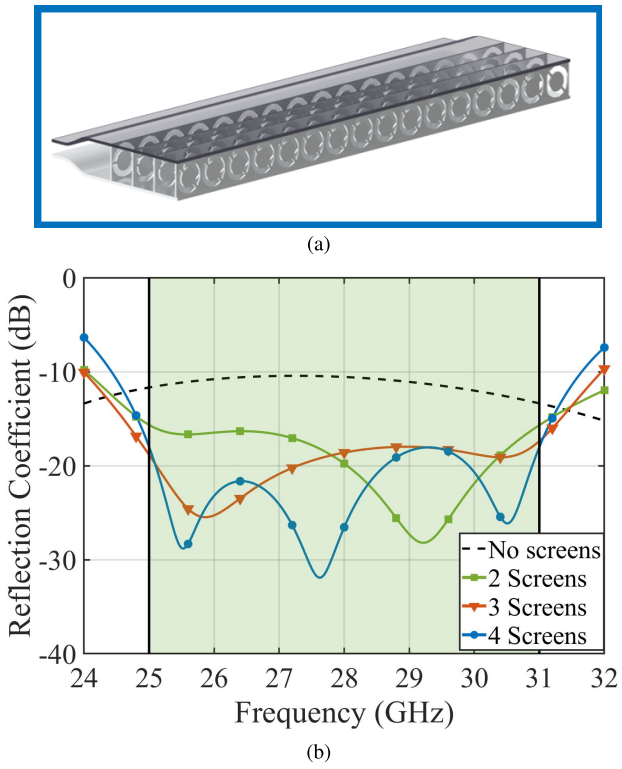

Fig. 8. Study of the required number of polarizer screens. (a) Case study when the PPW is loaded with four polarizer screens. (b) Reflection coefficient of the four case studies.

be noted that with this lateral dimension, the cutoff of the TE_{01} PPW mode is around 26 GHz, which means that this mode (horizontal polarization) is operating below cutoff. Therefore, in order not to suppress this mode in the PPW region between the screens, they must be closely spaced.

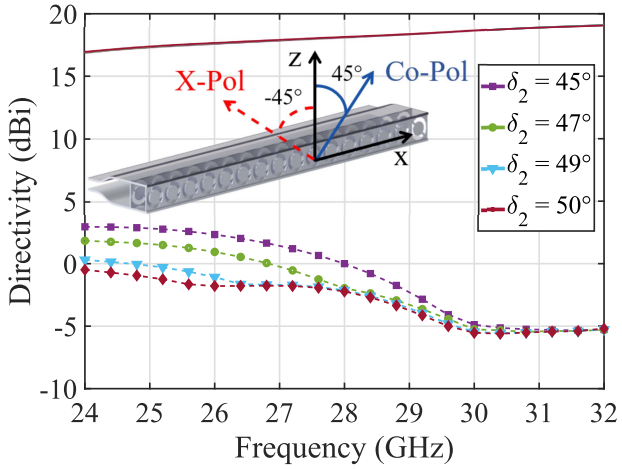

Fig. 9. Directivity of the co-pol (solid lines) and x-pol (dashed lines) of the radiating PPW loaded with two polarizer screens when varying δ_2.

The thickness of the perforated metal sheets, t, is chosen as 0.3 mm since at this thickness aluminum is still quite pliable and the sheets can, thereby, be bent into a circular shape without damage. For $n = 2$, 3, and 4, the rotation of the last polarizing screen is set to 45°. The rest of the parameters are then tuned to get the best matching over the frequency range. The reflection coefficients for the different numbers of screens are shown in Fig. 8(b). The best result is achieved with the highest number of screens, $n = 4$. However, decreasing the number of screens down to two still yields acceptable results, with a reflection coefficient which is below −15 dB over the frequency band of interest. Therefore, we continue with the design process using only two polarizer screens.

To estimate the performance of the polarizer screens, we study the far-field using Ludwig's third definition for co-polarization (co-pol) and cross-polarization (x-pol), which is suitable for a linear directional radiation pattern [44]. The inset of Fig. 9 defines the co-pol and x-pol. The parameters of the unit cell and screens were optimized, and their values are given in Table I. Fig. 9 shows a parametric sweep of the rotation angle of δ_2 at 45°, 47°, 49°, and 50° while keeping $\delta_1 = 29°$. The bar needs to be rotated more than 45° since the metallic plates in the z-direction suppress the TE_{01} mode, especially at the lowest frequency where this mode is in cutoff. By rotating δ_2 beyond 45°, it is possible to get a lower level of x-pol. Therefore, the chosen δ_2 is 50°.

The numerical results clearly indicate that the performance of the polarizer improves as the frequency increases. This is because the modal response becomes less dispersive when we move further away from the cutoff of the TE_{01} PPW mode. The overall x-pol level over the design frequency band could therefore be improved by increasing the unit cell height so that the TE_{01} PPW mode operates further away from cutoff. However, this would result in increased spacing between the antenna elements if the design is implemented in a vertically stacked antenna array, limiting beam steering in elevation.

D. Polarizer Under Oblique Incidence

The polarizer is intended to be installed conformally in the aperture of the PPW beamformer. As a result, the performance

TABLE I
FINAL DESIGN PARAMETERS OF CSSR POLARIZER SCREENS

Parameter	Dimension	Parameter	Dimension
P_x	5.7 mm	P_z	5.7 mm
S	2.65 mm	w	1 mm
g	0.43 mm	l_1	1.9 mm
δ_1	29°		

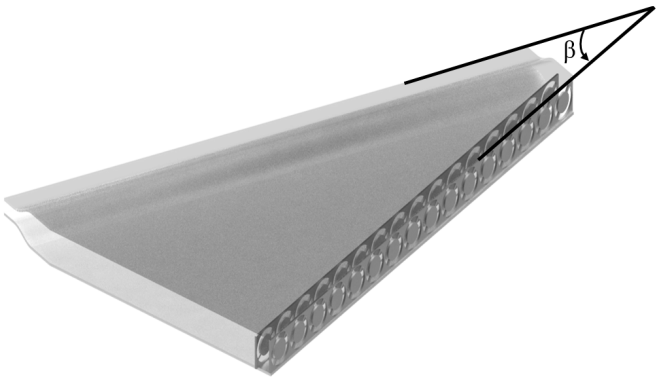

(a)

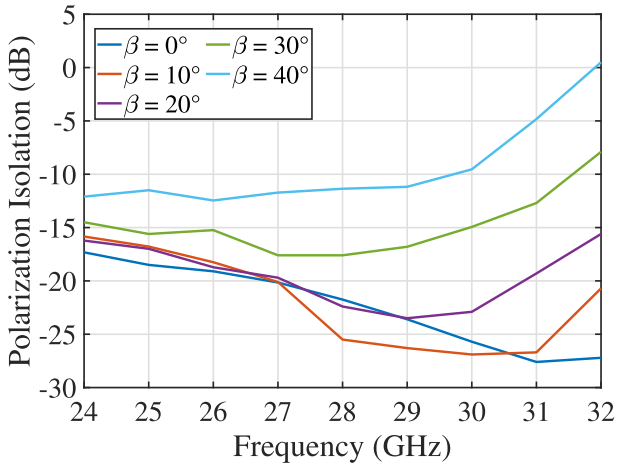

(b)

Fig. 10. (a) Rotated PPW model with loaded CSRRs. (b) Comparison between the polarization isolation of the rotated PPW model under different incident angles.

of the polarizer is not dependent on the scanning angle and is maintained when scanning to any direction. On the other hand, this implies that the polarizer partially operates under oblique incidence for all the scan angles, which may lead to reduced performance [45], [46]. To evaluate the performance under oblique incidence, we simulate the truncated planar polarizer that is rotated relative to the waveguide feed. The model used for the study is illustrated in Fig. 10(a). Specifically, we evaluate how rotation affects the polarization isolation under incident angles, β, from 0° to 40° in 10° steps. The polarization isolation is defined as the difference between the peak gains of the co-pol and x-pol in the -3 dB beamwidth of the main beam. The results of the study are shown in Fig. 10(b). We observe that the polarizer maintains the performance under incident angles up to $\beta = 20°$. At $\beta = 30°$, the performance at higher frequencies deteriorates as we observe that the polarization isolation is above -15 dB. At $\beta = 40°$, the polarizer is no longer performing as intended, with the polarization isolation above -15 dB over the whole frequency

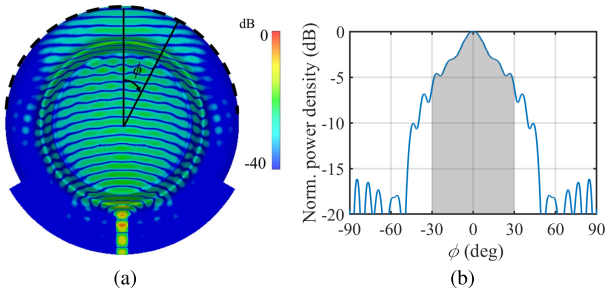

(a) (b)

Fig. 11. (a) Electric field distribution on the lens designed in Section II. (b) Normalized power density on the dashed line indicated in Fig. 11(a).

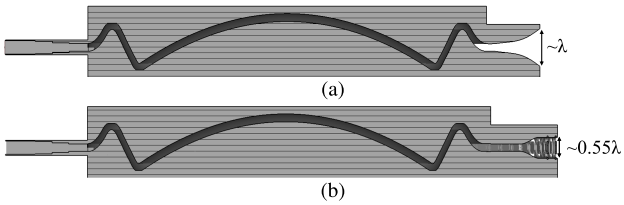

Fig. 12. Cross-sectional view of (a) lens antenna with an exponential flare and (b) lens antenna with polarizer screens loaded in the aperture.

range. With this study, we conclude that the angular stability of the polarizer is approximately ±30°.

Fig. 11 illustrates the electric field distribution in the lens designed in Section II when fed with port 6 at 28 GHz. We sample the power density on the dashed line as shown in Fig. 11(a). The dashed line corresponds to the position where the polarizer screens will be integrated in the final antenna design. We plot the result in Fig. 11(b). It is interesting to note that approximately 85% of the total power is confined within the ±30° range, corresponding to the shaded area in Fig. 11(b). This means that the majority of the power is incident at the polarizer with angles lower than 30°. This analysis provides further confidence in the operation of the conformal polarizer design prior to integration with the lens.

E. Comparison Between Antenna With a Flare and Polarizer Screens

In this section, we compare the simulation results of the antenna with a flare and the antenna with the polarizer in the aperture. As noted above, the vertical aperture size in the lens with the polarizer is smaller than that in the lens without the polarizer. To provide a fair comparison of the two antennas, we therefore compare the normalized radiation patterns. Fig. 12 shows a cross-sectional view of the two lenses, and Fig. 13 shows the simulation model and integration of the polarizer in the lens antenna. As illustrated in Fig. 13, the polarizer screens are bent to the shape of the lens and then placed between the top and bottom plates of the antenna.

Fig. 14(a) presents normalized radiation patterns for port 6 in the beamforming plane (H-plane) and the plane orthogonal to the beamforming plane (E-plane) at 28 GHz. As can be observed, the beamwidth in the H-plane is roughly the same for both the antennas. However, since the antenna with the radiating flare has a larger aperture in the E-plane than the antenna with polarizer screens, it has a narrower radiation pattern in this plane. In Fig. 14(b), it can be seen that the

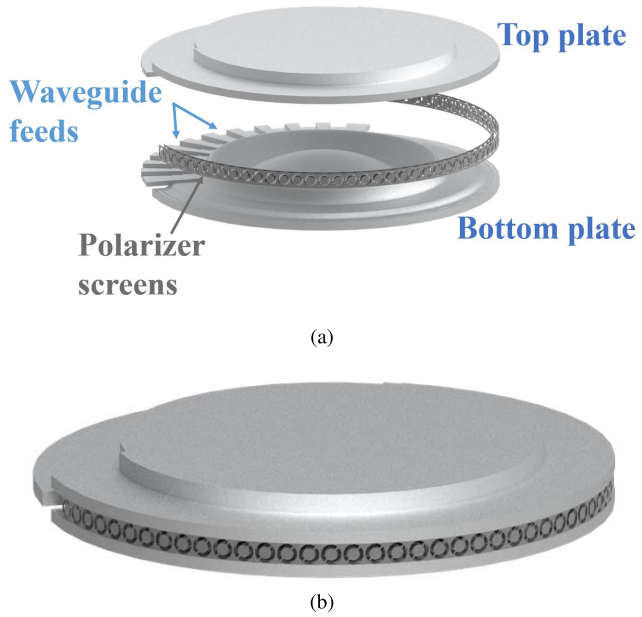

Fig. 13. Integration of the polarizer screens and the geodesic Luneburg lens. (a) Exploded view of the lens and polarizer. (b) Integrated device with the polarizer screens inserted into the flare of the antenna.

radiation efficiency for both the antennas is above 95%. In the same figure, we plot the 3 dB beamwidth in the H-plane of the two antennas when exciting the center port. The beamwidth of the two lenses is similar up to 30 GHz where we observe an increase in beamwidth for the antenna with polarizer screens. This is most likely due to phase aberrations caused by the polarizer screens.

IV. Experimental Results of the Fully Metallic Integrated Antenna and Polarizer

In this section, we present the simulations and experimental verification of the integrated lens antenna. The antenna is simulated using the *time-domain solver of CST Microwave Studio*. The polarizing screens are curved into a circular shape with a radius that matches the placement grooves allocated in the flare of the antenna. The manufactured prototype is shown in Fig. 15. Fig. 15(a) shows the top and bottom plates of the geodesic lens antenna before assembly with the polarizer screens placed in the bottom plate. The two plates that form the geodesic surface were manufactured using CNC milling, and the polarizing screens were manufactured by water-jet cutting aluminum sheets. Fig. 15(b) illustrates the assembled antenna during measurements in the anechoic chamber at KTH Royal Institute of Technology.

The measured and simulated reflection coefficients are represented in Fig. 16(a). The measured reflection coefficients are below -10 dB in the frequency band of interest, but are a bit higher than the simulated results, below -15 dB. The measured and simulated port-to-port coupling between selected ports are depicted in Fig. 16(b). Similar levels of port-to-port coupling are obtained from the measurement and simulation with most of the values below -20 dB. The measured and simulated normalized radiation patterns of the co-pol, in the scanning plane at 25, 28, and 31 GHz are depicted in Fig. 17. There is a good agreement between the simulated and measured results, especially at 25 and 28 GHz. In the measurements, the beamwidth at 31 GHz slightly increases.

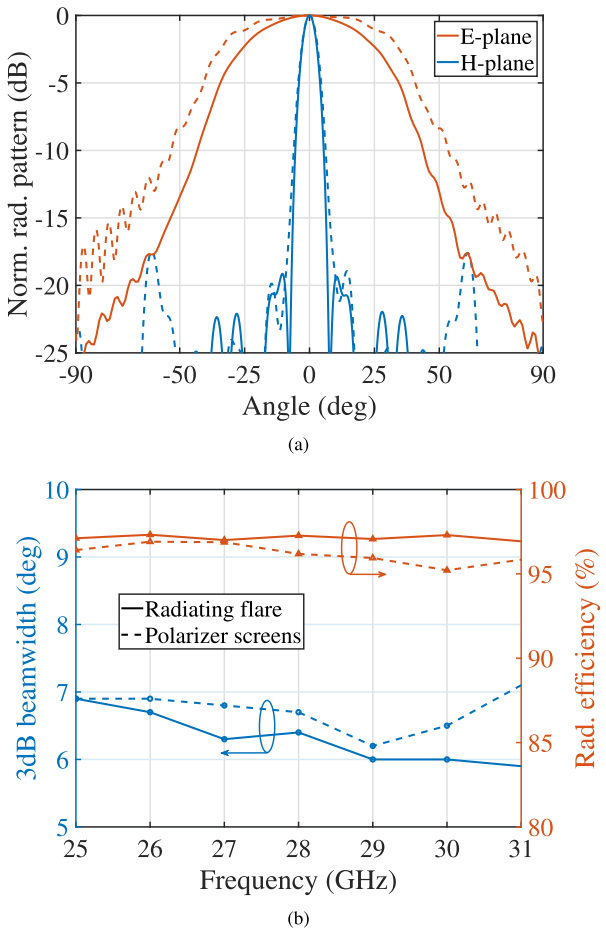

Fig. 14. (a) Normalized radiation pattern in the E- and H-planes of port 6 for the antenna with an exponential flare (solid lines) and the antenna with polarizers loaded in the aperture (dashed lines) at 28 GHz. (b) Comparison between the simulated radiation efficiency and 3 dB beamwidth of the two antenna designs when exciting port 6.

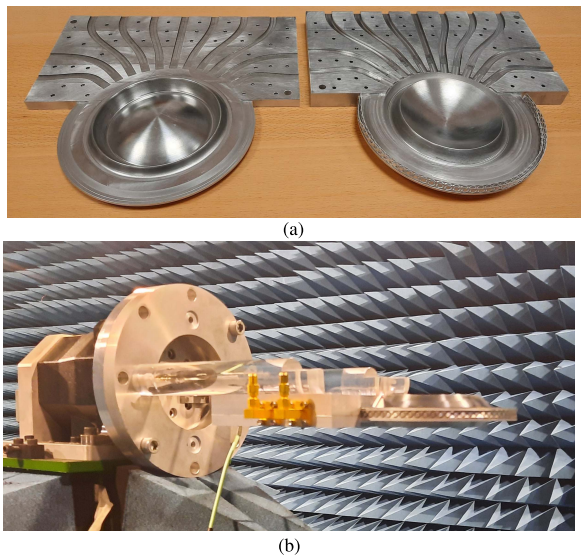

Fig. 15. (a) Bottom and top plates of the manufactured antenna. (b) Assembled antenna during measurements in the anechoic chamber at KTH.

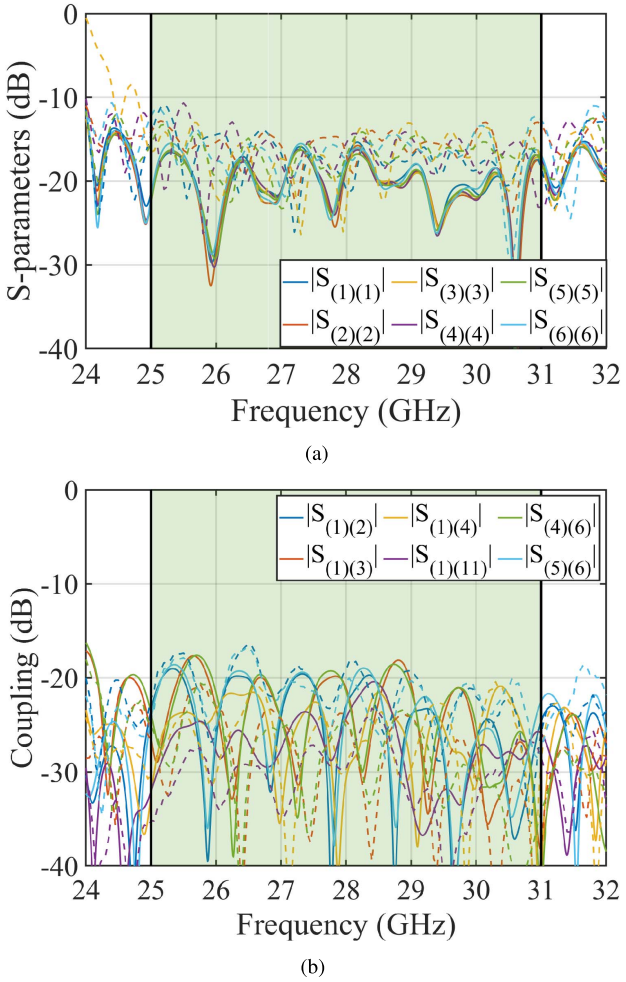

Fig. 16. Simulated (solid lines) and measured (dashed lines) of (a) reflection coefficients for ports 1–6 and (b) selected port-to-port coupling.

The sidelobe levels in both the simulations and measurements are below −15 dB for all the ports at 25 and 28 GHz. Slightly higher side lobes are observed at 31 GHz but always below −13 dB.

The measured and simulated peak gains of ports 5, 6, 8, and 11 are shown in Fig. 18(a). Although omitted here, the other ports had a similar performance. The gain is stable between ports although some differences are noticeable between the measured and simulated results. This discrepancy is due to the surface roughness of the materials. A simulation with a root mean square (Rq) surface roughness of 5 μm is illustrated in Fig. 18(a), demonstrating a good agreement with the measurements.

Port 6 experienced more losses than port 1, especially at 31 GHz. The main difference between these two ports is in the waveguide length, which for port 6 is substantially longer. The longer the waveguide, the higher the undesired leakage and material losses due to surface roughness. It is important to note that the waveguides are only for testing purposes. In a real implementation, these waveguides are not necessary since the lens will be directly connected to the PCB.

Fig. 18(b) presents the polarization isolation of the integrated antenna. The isolation obtained with the truncated planar polarizer (Fig. 9) is included as reference. The polarization

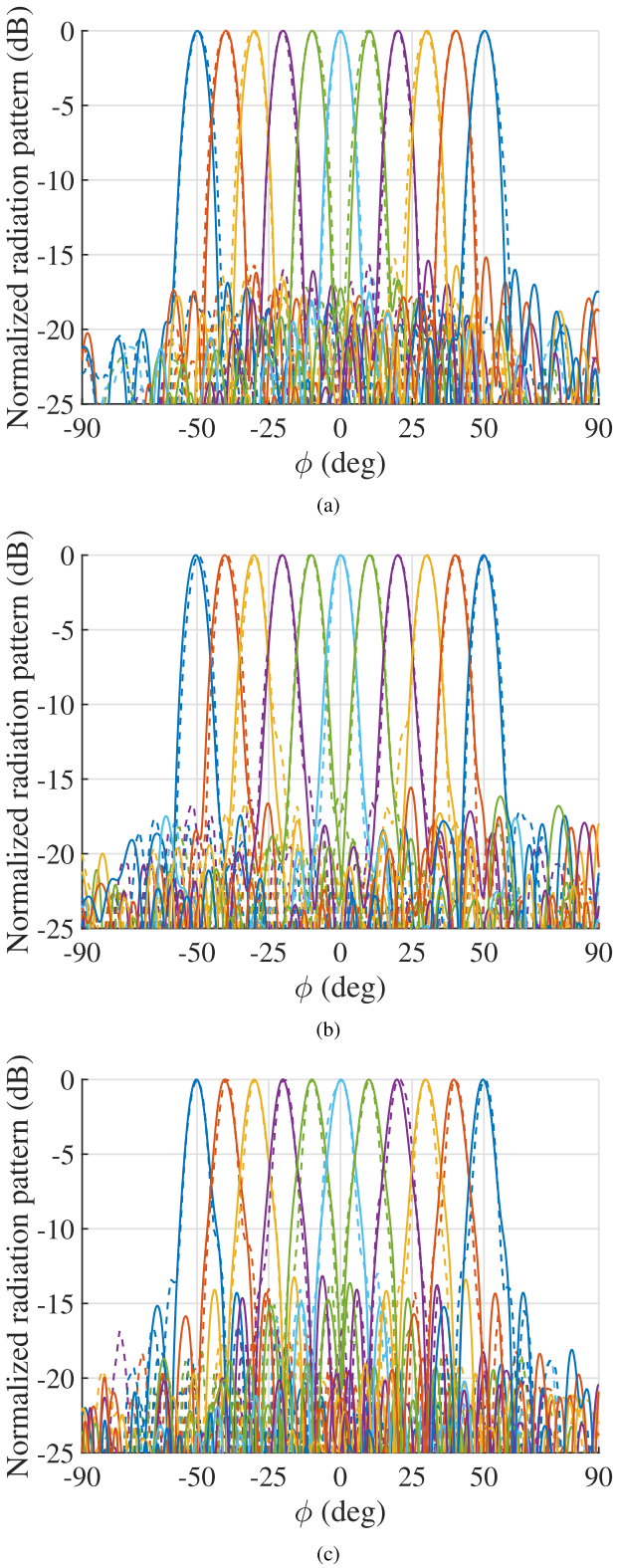

Fig. 17. Normalized radiation pattern for the simulated antenna (solid lines) and measured prototype (dashed lines) of the 11 ports at (a) 25, (b) 28, and (c) 31 GHz.

isolation of the antenna is defined in the same manner as in Section III. Good agreement is observed between the x-pol of the truncated planar polarizer and the simulated and measured x-pol levels in the integrated lens antenna. The polarization isolation is below −18 dB over the whole frequency range

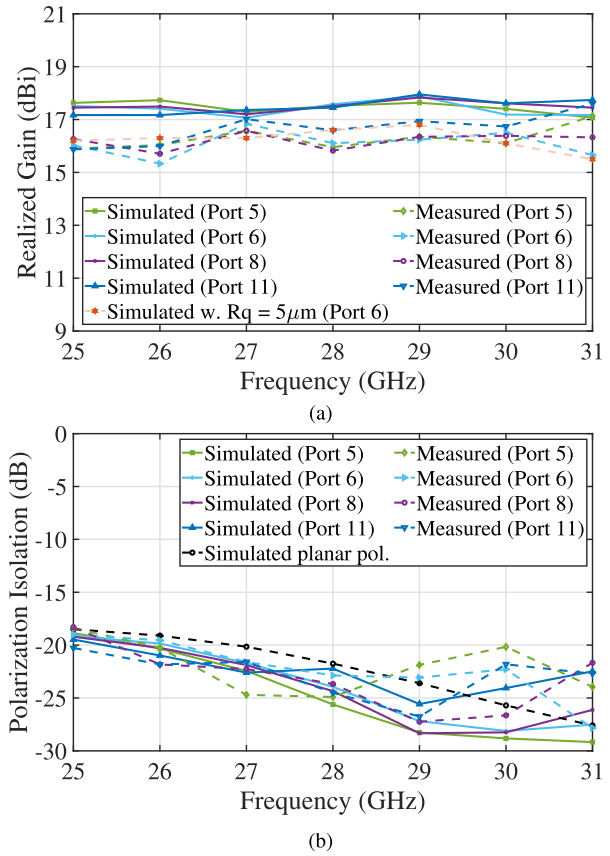

Fig. 18. (a) Simulated and measured peak gains. (b) Simulated and measured polarization isolation.

and mostly below −20 dB in both the simulations and measurements.

V. Conclusion

A fully metallic and low-profile method to achieve polarization transformation in a geodesic Luneburg lens antenna has been proposed and validated experimentally. The polarization transformation is achieved by placing two metallic screens of CSRRs in the aperture of the antenna. The polarizing screens rotate the electric field from a vertical linear polarization to a linear +45° polarization while providing a good impedance matching to free space. Since the screens are placed conformally in the aperture of the antenna, the antenna performance is unaffected when the beam is steered in the angular range of ±50°.

The proposed concept can be extended to design PPW antennas that generate circular polarization by replacing the linear-to-linear polarizer with a linear-to-circular polarizer similar to the designs in [32], [47], and [48]. To the authors' best knowledge, no polarizer design, applicable for a PPW beamformer, has been reported that transforms the polarization while providing impedance matching to free space. In addition, the reported designs on low-profile polarization transformation in PPW beamformer suffer from either limited bandwidth or limited scanning range [38], [39] which is not the case for the proposed design.

The integrated antenna operates at a center frequency of 28 GHz with over 20% bandwidth having measured reflection coefficients below −10 dB, a port-to-port coupling below −18 dB, and a measured peak gain of 17.6 dBi. Good agreement is achieved between the measured and simulated radiation patterns, apart from slightly lower gain observed in measurements. The lower gain is attributed to the surface roughness of the metal, which was not considered in the simulations. The antenna supports a beam scanning of ±50°, which is demonstrated with 11 discrete beams with 10° separation.

By vertically stacking the proposed integrated antenna, polarization diversity can be exploited by mirroring the polarizing screens in the antennas. One of the antennas would then radiate a +45° polarized wave, while the other one a −45° polarized wave. Furthermore, the presented design has an aperture height of 0.55λ, and as a result, 2-D beam steering (switching in azimuth and scanning in elevation) is enabled by stacking antennas with the same polarization. For the 2-D beam steering antenna stack, the polarization diversity can be exploited using two independent systems, one for each polarization. Although the polarization technique proposed in this article was only applied to a geodesic Luneburg lens, it is general and it can be applied to both flat PPW lenses and other versions of conformal beamformers.

References

[1] E. Björnson, J. Hoydis, and L. Sanguinetti, "Massive MIMO networks: Spectral, energy, and hardware efficiency," *Found. Trends Signal Process.*, vol. 11, nos. 3–4, pp. 154–655, 2017.

[2] A. Osseiran, S. Parkvall, P. Persson, A. Zaidi, S. Magnusson, and K. Balachandran. (Apr. 2020). *5G Wireless Access: An Overview*. Accessed: May 31, 2021. [Online]. Available: https://www.ericsson.com/en/reports-and-papers/white-papers/5g-wireless-access-an-overview

[3] G. Wikström. (Nov. 2020). *Ever-Present Intelligent Communication*. Accessed: May 31, 2022. [Online]. Available: https://www.ericsson.com/en/reports-and-papers/white-papers/a-research-outlook-towards-6g

[4] Y. J. Guo, M. Ansari, R. Ziolkowski, and N. J. G. Fonseca, "Quasi-optical multi-beam antenna technologies for B5G and 6G mmWave and THz networks: A review," *IEEE Open J. Antennas Propag.*, vol. 2, pp. 807–830, 2021.

[5] S. Rangan, T. S. Rappaport, and E. Erkip, "Millimeter-wave cellular wireless networks: Potentials and challenges," *Proc. IEEE*, vol. 102, no. 3, pp. 366–385, Mar. 2014.

[6] F. Rusek et al., "Scaling up MIMO: Opportunities and challenges with very large arrays," *IEEE Signal Process. Mag.*, vol. 30, no. 1, pp. 40–60, Jan. 2013.

[7] C.-X. Mao, S. Gao, and Y. Wang, "Broadband high-gain beam-scanning antenna array for millimeter-wave applications," *IEEE Trans. Antennas Propag.*, vol. 65, no. 9, pp. 4864–4868, Sep. 2017.

[8] J. Herranz-Herruzo et al., "LOCOMO SatCom terminal: A switchable RHCP/LHCP array antenna for on-the-move applications in Ka-band," in *Proc. IEEE Int. Symp. Antennas Propag. USNC/URSI Nat. Radio Sci. Meeting*, Jul. 2015, pp. 210–211.

[9] F. Tiezzi, S. Vaccaro, D. Llorens, C. Dominguez, and M. Fajardo, "Ku-band hybrid phased array antennas for mobile satellite communication systems," in *Proc. 7th Eur. Conf. Antennas Propag. (EuCAP)*, Apr. 2013, pp. 1605–1608.

[10] A. Natarajan, A. Komijani, and A. Hajimiri, "A fully integrated 24-GHz phased-array transmitter in CMOS," *IEEE J. Solid-State Circuits*, vol. 40, no. 12, pp. 2502–2514, Dec. 2005.

[11] W. Rotman, "Wide-angle scanning with microwave double-layer pillboxes," *IRE Trans. Antennas Propag.*, vol. 6, no. 1, pp. 96–105, Jan. 1958.

[12] W. E. Kock, "Metallic delay lenses," *Bell Syst. Tech. J.*, vol. 27, no. 1, pp. 58–82, Jan. 1948.

[13] E. D. Sharp, "Electromagnetic theory of wire-grid lens HF antenna," *IEEE Trans. Antennas Propag.*, vol. AP-13, no. 5, pp. 703–709, Sep. 1965.

[14] O. Quevedo-Teruel, M. Ebrahimpouri, and F. Ghasemifard, "Lens antennas for 5G communications systems," *IEEE Commun. Mag.*, vol. 56, no. 7, pp. 36–41, Jul. 2018.

[15] R. K. Luneburg and M. Herzberger, "*Mathematical Theory of Optics*. Renton, WA, USA: Providence, 1944, p. 391.

[16] F. Fan, M. Cai, J. Zhang, Z. Yan, and J. Wu, "Wideband low-profile Luneburg lens based on a glide-symmetric metasurface," *IEEE Access*, vol. 8, pp. 85698–85705, 2020.

[17] G. Peeler and D. Archer, "A two-dimensional microwave Luneberg lens," *Trans. IRE Prof. Group Antennas Propag.*, vol. 1, no. 1, pp. 12–23, Jun. 1953.

[18] M. Bosiljevac, M. Casaletti, F. Caminita, Z. Sipus, and S. Maci, "Non-uniform metasurface Luneburg lens antenna design," *IEEE Trans. Antennas Propag.*, vol. 60, no. 9, pp. 4065–4073, Sep. 2012.

[19] A. Dhouibi, S. N. Burokur, A. D. Lustrac, and A. Priou, "Low-profile substrate-integrated lens antenna using metamaterials," *IEEE Antennas Wireless Propag. Lett.*, vol. 12, pp. 43–46, 2013.

[20] J. Dockrey, M. J. Lockyear, S. Berry, S. Horsley, J. R. Sambles, and A. P. Hibbins, "Thin metamaterial Luneburg lens for surface waves," *Phys. Rev. B, Condens. Matter*, vol. 87, no. 12, Mar. 2013, Art. no. 125137.

[21] O. Zetterstrom, R. Hamarneh, and O. Quevedo-Teruel, "Experimental validation of a metasurface Luneburg lens antenna implemented with glide-symmetric substrate-integrated holes," *IEEE Antennas Wireless Propag. Lett.*, vol. 20, no. 5, pp. 698–702, May 2021.

[22] M. Šarbort and T. Tyc, "Multi-focal spherical media and geodesic lenses in geometrical optics," *J. Opt.*, vol. 15, no. 12, Oct. 2013, Art. no. 125716.

[23] Q. Liao, N. J. G. Fonseca, and O. Quevedo-Teruel, "Compact multibeam fully metallic geodesic Luneburg lens antenna based on non-Euclidean transformation optics," *IEEE Trans. Antennas Propag.*, vol. 66, no. 12, pp. 7383–7388, Dec. 2018.

[24] N. J. G. Fonseca, Q. Liao, and O. Quevedo-Teruel, "Equivalent planar lens ray-tracing model to design modulated geodesic lenses using non-Euclidean transformation optics," *IEEE Trans. Antennas Propag.*, vol. 68, no. 5, pp. 3410–3422, May 2020.

[25] N. J. G. Fonseca, Q. Liao, and O. Quevedo-Teruel, "Compact parallel-plate waveguide half-Luneburg geodesic lens in the Ka-band," *IET Microw., Antennas Propag.*, vol. 15, no. 2, pp. 123–130, Feb. 2021.

[26] O. Quevedo-Teruel et al., "Geodesic lens antennas for 5G and beyond," *IEEE Commun. Mag.*, vol. 60, no. 1, pp. 40–45, Jan. 2022.

[27] R. C. Mitchell-Thomas, O. Quevedo-Teruel, T. M. McManus, S. A. R. Horsley, and Y. Hao, "Lenses on curved surfaces," *Opt. Lett.*, vol. 39, no. 12, pp. 3551–3554, Jun. 2014.

[28] S. Horsley, I. Hooper, R. Mitchell-Thomas, and O. Quevedo-Teruel, "Removing singular refractive indices with sculpted surfaces," *Sci. Rep.*, vol. 4, no. 1, p. 4876, May 2014.

[29] R. Rinehart, "A solution of the problem of rapid scanning for radar antennae," *J. Appl. Phys.*, vol. 19, no. 9, pp. 860–862, Sep. 1948.

[30] K. S. Kunz, "Propagation of microwaves between a parallel pair of doubly curved conducting surfaces," *J. Appl. Phys.*, vol. 25, no. 5, pp. 642–653, May 1954.

[31] N. J. G. Fonseca and C. Mangenot, "High-performance electrically thin dual-band polarizing reflective surface for broadband satellite applications," *IEEE Trans. Antennas Propag.*, vol. 64, no. 2, pp. 640–649, Feb. 2016.

[32] J. Lundgren, O. Zetterstrom, F. Mesa, N. J. G. Fonseca, and O. Quevedo-Teruel, "Fully metallic dual-band linear-to-circular polarizer for K/K_a-band," *IEEE Antennas Wireless Propag. Lett.*, vol. 20, no. 11, pp. 2191–2195, Nov. 2021.

[33] K. X. Wang and H. Wong, "Design of a wideband circularly polarized millimeter-wave antenna with an extended hemispherical lens," *IEEE Trans. Antennas Propag.*, vol. 66, no. 8, pp. 4303–4308, Aug. 2018.

[34] M. A. Campo, G. Carluccio, D. Blanco, O. Litschke, S. Bruni, and N. Llombart, "Wideband circularly polarized antenna with in-lens polarizer for high-speed communications," *IEEE Trans. Antennas Propag.*, vol. 69, no. 1, pp. 43–54, Jan. 2021.

[35] S. Mercader-Pellicer, W. Tang, D. Bresciani, H. Legay, N. J. G. Fonseca, and G. Goussetis, "Angularly stable linear-to-circular polarizing reflectors for multiple beam antennas," *IEEE Trans. Antennas Propag.*, vol. 69, no. 8, pp. 4380–4389, Aug. 2021.

[36] Ericsson AB. *Lightpole Site Slim—An Innovative Small Cell Solution*. Accessed: Mar. 14, 2021. [Online]. Available: https://www.ericsson.com/en/small-cells/outdoor-coverage/lightpole-site-slim

[37] M. Chen and G. Tsandoulas, "A wide-band square-waveguide array polarizer," *IEEE Trans. Antennas Propag.*, vol. AP-21, no. 3, pp. 389–391, May 1973.

[38] N. Bartolomei et al., "Circularly polarized parallel plate waveguide multiple-beam lens-like antenna for satcom applications," in *Proc. 13th Eur. Conf. Antennas Propag. (EuCAP)*, Mar. 2019, pp. 1–3.

[39] J. P. Mahon. *Parallel Plate Septum Polarizer for Low Profile Antenna Applications*. Accessed: Mar. 1, 20225. [Online]. Available: https://patents.google.com/patent/US6861997B2/en

[40] F. Doucet et al., "Shaped continuous parallel plate delay lens with enhanced scanning performance," *IEEE Trans. Antennas Propag.*, vol. 67, no. 11, pp. 6695–6704, Nov. 2019.

[41] M. Ettorre, R. Sauleau, and L. Le Coq, "Multi-beam multi-layer leaky-wave SIW pillbox antenna for millimeter-wave applications," *IEEE Trans. Antennas Propag.*, vol. 59, no. 4, pp. 1093–1100, Apr. 2011.

[42] O. Dahlberg, G. Valerio, and O. Quevedo-Teruel, "Fully metallic flat lens based on locally twist-symmetric array of complementary split-ring resonators," *Symmetry*, vol. 11, no. 4, p. 581, 2019.

[43] Z. Wei, Y. Cao, Y. Fan, X. Yu, and H. Li, "Broadband polarization transformation via enhanced asymmetric transmission through arrays of twisted complementary split-ring resonators," *Appl. Phys. Lett.*, vol. 99, no. 22, p. 221907, Nov. 2011.

[44] A. Ludwig, "The definition of cross polarization," *IEEE Trans. Antennas Propag.*, vol. AP-21, no. 1, pp. 116–119, Jan. 1973.

[45] H. B. Wang and Y. J. Cheng, "Single-layer dual-band linear-to-circular polarization converter with wide axial ratio bandwidth and different polarization modes," *IEEE Trans. Antennas Propag.*, vol. 67, no. 6, pp. 4296–4301, Jun. 2019.

[46] W. Zhang, J.-Y. Li, and J. Xie, "A broadband circular polarizer based on cross-shaped composite frequency selective surfaces," *IEEE Trans. Antennas Propag.*, vol. 65, no. 10, pp. 5623–5627, Oct. 2017.

[47] J. D. Baena, S. B. Glybovski, J. P. del Risco, A. P. Slobozhanyuk, and P. A. Belov, "Broadband and thin linear-to-circular polarizers based on self-complementary zigzag metasurfaces," *IEEE Trans. Antennas Propag.*, vol. 65, no. 8, pp. 4124–4133, Aug. 2017.

[48] M. D. Mastro, M. Ettorre, and A. Grbic, "Dual-band, orthogonally-polarized LP-to-CP converter for SatCom applications," *IEEE Trans. Antennas Propag.*, vol. 68, no. 9, pp. 6764–6776, Sep. 2020.

Freysteinn V. Vidarsson (Graduate Student Member, IEEE) received the B.Sc. degree in mechatronics engineering from Reykjavik University, Reykjavik, Iceland, in 2018, and the M.Sc. degree in electrical and electromagnetic engineering from KTH Royal Institute of Technology, Stockholm, Sweden, in 2020, where he is currently pursuing the Ph.D. degree in antennas and electromagnetics at the Division of Electromagnetic Engineering.

His research is focused on geodesic lens antennas for satellite and terrestrial communications.

Oskar Zetterstrom (Graduate Student Member, IEEE) received the B.Sc., M.Sc., and Licentiate degrees in electrical and electromagnetic engineering from the KTH Royal Institute of Technology, Stockholm, Sweden, in 2016, 2019, and 2021, respectively, where he is currently pursuing the Ph.D. degree on antennas and electromagnetics with the Division of Electromagnetic Engineering.

He has authored or coauthored over 60 peer-reviewed journals and conference papers. His research has been focused on transformation optics, lens antennas, metamaterials possessing higher symmetries, and leaky-wave antennas

Mr. Zetterstrom is a member of the newly formed EurAAP Working Group for Early Careers in Antennas and Propagation (ECAP). He has been awarded the first price in the Student Design Competition at APS/URSI in 2016, the Best Student Paper Award at URSI Spain in 2020, and the Best Antenna Technology Paper Award at EuCAP 2022 for his works.

Astrid Algaba-Brazález received the Telecommunication Engineering degree from the Miguel Hernández University of Elche, Alicante, Spain, in 2009, and the Licentiate of Engineering and Ph.D. degrees from the Chalmers University of Technology, Gothenburg, Sweden, in 2013 and 2015, respectively.

She joined Ericsson Research, Gothenburg, in November 2014. She currently works as a Senior Researcher with the Antenna and Microwave Hardware Unit with special focus on 5G and 6G antenna hardware activities. She has also been leading all research activities related to metasurfaces within Ericsson Research since 2015. Her research interests include millimeter and submillimeter antenna array technologies, lens antennas, design of microwave passive components such as filters, metasurfaces, integration of active components and antennas at millimeter-wave frequencies, and design of interconnects and transitions to achieve such integration.

Dr. Algaba-Brazález received the second Best Paper Award at the International Symposium on Antennas and Propagation (ISAP) in 2017 and the Best Paper Award in Antennas at the European Conference on Antennas and Propagation (EuCAP) in 2020.

Nelson J. G. Fonseca (Senior Member, IEEE) received the M.Eng. degree from the Ecole Nationale Supérieure d'Electrotechnique, Electronique, Informatique, Hydraulique et Télécommunications (ENSEEIHT), Toulouse, France, in 2003, the M.Sc. degree from the Ecole Polytechnique de Montreal, Montreal, QC, Canada, in 2003, and the Ph.D. degree from the Institut National Polytechnique de Toulouse—Université de Toulouse, Toulouse, in 2010, all in electrical engineering.

He currently works as an Antenna Engineer with the Antenna and Sub-Millimetre Waves Section, European Space Agency (ESA), Noordwijk, The Netherlands. Since November 2020, he also holds an Honorary Appointment as a Professional Fellow at the University of Technology Sydney (UTS), Sydney, NSW, Australia. His research interests include multiple beam antennas for space missions, beam-former theory and design, ground terminal antennas, transfer of technology from and to terrestrial systems, including 5G networks, and novel manufacturing techniques. He has authored or coauthored more than 260 articles in peer-reviewed journals and conferences, and holds over 50 patents issued or pending.

Dr. Fonseca has been a Board Member of the European School of Antennas and Propagation (ESoA) since January 2019 and is also serving as a Coordinator of the ESA/ESoA course on Antennas for Space Applications, for which he was voted the best lecturer by the participants of the 2020 edition. He is the elected EurAAP Regional Delegate representing Benelux from 2021 to 2023. He received several prizes and awards, including the Best Young Engineer Paper Award at the 29th ESA Workshop on Antennas in 2007, the ESA Teamwork Excellence Award in 2020, the multiple ESA Technical Improvement Awards, and the Best Applied Technology Antenna Paper Award at EuCAP in 2022. He is also serving as the Chair for the IEEE MTT-S Technical Committee 29 (TC-29) on Microwave Aerospace Systems. He is currently serving as an Associate Editor for the *IET Microwaves, Antennas and Propagation* (MAP) and IEEE TRANSACTIONS ON MICROWAVE THEORY AND TECHNIQUES (TMTT), and as a Topic Editor for IEEE JOURNAL OF MICROWAVES (JMW).

Martin Johansson (Senior Member, IEEE) received the M.Sc. degree in engineering physics and the Ph.D. degree in electromagnetics from the Chalmers University of Technology, Gothenburg, Sweden, in 1986 and 1997, respectively.

He joined Ericsson Research, Ericsson AB, Gothenburg, in 1997, where he currently serves as an expert in antenna technology. His current research interests include antenna technology for mobile communications, antenna system modeling, and deterministic channel modeling.

Lars Manholm received the M.Sc. degree in electrical engineering and the Licentiate of Technology degree in electromagnetics from the Chalmers University of Technology, Gothenburg, Sweden, in 1994 and 1998, respectively.

He joined Ericsson Microwave Systems, Gothenburg, as an Antenna Designer, in 1998, and Ericsson Research, Gothenburg, in 2003, where he was a Master Researcher in antenna hardware. His research interests include electronically steerable antennas and antenna arrays for cellular base station and fixed radio link applications at microwave and millimeter-wave frequencies.

Oscar Quevedo-Teruel (Senior Member, IEEE) received the Telecommunication Engineering and Ph.D. degrees from the Carlos III University of Madrid, Madrid, Spain, in 2005 and 2010, respectively.

From 2010 to 2011, he joined the Department of Theoretical Physics of Condensed Matter, Universidad Autonoma de Madrid, Madrid, as a Research Fellow and went on to continue his post-doctoral research at the Queen Mary University of London, London, U.K., from 2011 to 2013. In 2014, he joined the Division of Electromagnetic Engineering, School of Electrical Engineering and Computer Science, KTH Royal Institute of Technology, Stockholm, Sweden, where he is a Professor and the Director of the Master Programme in Electromagnetics Fusion and Space Engineering. He is the coauthor of more than 110 articles in international journals and 180 at international conferences.

Dr. Quevedo-Teruel has been a member of the EurAAP Board of Directors since January 2021. He was a Distinguished Lecturer of the IEEE Antennas and Propagation Society from 2019 to 2021. He has also been the Chair of the IEEE APS Educational Initiatives Programme since 2020. He has made scientific contributions to higher symmetries, transformation optics, lens antennas, metasurfaces, leaky-wave antennas, and high-impedance surfaces. He has been an Associate Editor of the IEEE TRANSACTIONS ON ANTENNAS AND PROPAGATION since 2018 and has been the Founder and the Editor-in-Chief of the *EurAAP Journal Reviews of Electromagnetics* since 2020. He was the EurAAP delegate for Sweden, Norway, and Iceland from 2018 to 2020. Since January 2022, he has been the Vice-Chair of EurAAP.